Icarus 221 (2012) 276–288

Contents lists available at SciVerse ScienceDirect

Icarus

journal homepage: www.elsevier.com/locate/icarus

The impact of resolution on the dynamics of the martian global atmosphere: Varying resolution studies with the MarsWRF GCM

Anthony D. Toigo [a,*], Christopher Lee [b], Claire E. Newman [b], Mark I. Richardson [b]

[a] The Johns Hopkins University Applied Physics Laboratory, 11100 Johns Hopkins Road, Laurel, MD 20723, United States
[b] Ashima Research, 600 S. Lake Ave., Suite 104, Pasadena, CA 91106, United States

ARTICLE INFO

Article history:
Received 13 March 2012
Revised 16 July 2012
Accepted 21 July 2012
Available online 1 August 2012

Keywords:
Mars, Climate
Mars, Atmosphere
Meteorology
Atmospheres, Dynamics

ABSTRACT

We investigate the sensitivity of the circulation and thermal structure of the martian atmosphere to numerical model resolution in a general circulation model (GCM) using the martian implementation (MarsWRF) of the planetWRF atmospheric model. We provide a description of the MarsWRF GCM and use it to study the global atmosphere at horizontal resolutions from 7.5° × 9° to 0.5° × 0.5°, encompassing the range from standard Mars GCMs to global mesoscale modeling. We find that while most of the gross-scale features of the circulation (the rough location of jets, the qualitative thermal structure, and the major large-scale features of the surface level winds) are insensitive to horizontal resolution over this range, several major features of the circulation are sensitive in detail. The northern winter polar circulation shows the greatest sensitivity, showing a continuous transition from a smooth polar winter jet at low resolution, to a distinct vertically "split" jet as resolution increases. The separation of the lower and middle atmosphere polar jet occurs at roughly 10 Pa, with the split jet structure developing in concert with the intensification of meridional jets at roughly 10 Pa and above 0.1 Pa. These meridional jets appear to represent the separation of lower and middle atmosphere mean overturning circulations (with the former being consistent with the usual concept of the "Hadley cell"). Further, the transition in polar jet structure is more sensitive to changes in zonal than meridional horizontal resolution, suggesting that representation of small-scale wave-mean flow interactions is more important than fine-scale representation of the meridional thermal gradient across the polar front. Increasing the horizontal resolution improves the match between the modeled thermal structure and the Mars Climate Sounder retrievals for northern winter high latitudes. While increased horizontal resolution also improves the simulation of the northern high latitudes at equinox, even the lowest model resolution considered here appears to do a good job for the southern winter and southern equinoctial pole (although in detail some discrepancies remain). These results suggest that studies of the northern winter jet (e.g., transient waves and cyclogenesis) will be more sensitive to global model resolution that those of the south (e.g., the confining dynamics of the southern polar vortex relevant to studies of argon transport). For surface winds, the major effect of increased horizontal resolution is in the superposition of circulations forced by local-scale topography upon the large-scale surface wind patterns. While passive predictions of dust lifting are generally insensitive to model horizontal resolution when no lifting threshold is considered, increasing the stress threshold produces significantly more lifting in higher resolution simulations with the generation of finer-scale, higher-stress winds due primarily to better-resolved topography. Considering the positive feedbacks expected for radiatively active dust lifting, we expect this bias to increase when such feedbacks are permitted.

1. Introduction

Global scale modeling of the martian atmospheric circulation began almost half a century ago with the earliest forms of general circulation models (GCMs) (Leovy and Mintz, 1969). From the outset, the horizontal resolution of the models has been determined by the goal of simulating steady and transient motions thought to be of dominant importance to the general circulation, with the radius of deformation in mid-latitudes guiding the choice of this minimum resolution. Since the 1960s, the resolution of published model results has remained within the range of 5–7.5° in latitude and 5–9° in longitude, corresponding to about 300–550 km spacing of grid points at the equator. As computing

* Corresponding author.
E-mail addresses: Anthony.Toigo@jhuapl.edu (A.D. Toigo), lee@ashimaresearch.com (C. Lee), claire@ashimaresearch.com (C.E. Newman), mir@ashimaresearch.com (M.I. Richardson).

0019-1035/$ - see front matter © 2012 Elsevier Inc. All rights reserved.
http://dx.doi.org/10.1016/j.icarus.2012.07.020

power has increased, the models have instead tended to see greater extent and resolution in the vertical (from about 50 km to over 80 km in vertical extent, with layer numbers increasing from 2 to over 40) and dramatic increases in the complexity and duration of simulations (from the seasonal simulations of Pollack et al. (1990) and Haberle et al. (1993) to current multi-decadal simulations).

Synoptic-scale Mars GCM simulations perform reasonably well when compared to large-scale spacecraft observations and lander surface pressure observations, hence the persistence of this resolution choice. However, as computational power now makes higher resolution global simulations possible, although increasingly resource demanding, it is worth contemplating the potential differences between global synoptic (hundreds of kilometers horizontal resolution) and global mesoscale (tens of kilometers horizontal resolution) simulations of the martian atmosphere. Indeed, a number of areas of martian atmospheric and climate dynamics may be rather sensitive to scale of resolution. For example, initial dust lifting events tend to be on the microscale and mesoscale and hence significant questions remain about how well a synoptic scale model can really do in regard to capturing dust storm origins and variability. Other questions focus on the degree to which mesoscale circulations associated with enormous topographic features like Olympus Mons and the Hellas Basin rims contribute directly and significantly to the global scale circulation or global transport of water and dust (Rafkin et al., 2002; Michaels et al., 2006).

In this study, we use the martian version (MarsWRF) of the planetary Weather Research and Forecasting (planetWRF) model (www.planetwrf.com) to examine the impact of resolution choice on the representation of the general circulation, the polar vortex, atmospheric waves, and the nature of near surface winds and wind stresses of significance for dust lifting. This paper is divided into several parts. In Section 2, we provide an introduction and discussion of MarsWRF and its use as a GCM. In Section 3, we present a suite of simulations with the MarsWRF GCM at a range of resolutions differing by up to an order of magnitude and describe their zonal mean characteristics. In Section 4, we discuss the changes in atmospheric waves represented by the model as resolution is changed. In Section 5, we proceed to examine how resolution variations affect surface wind distributions and wind stresses with a view to assessing the likely impact of resolution on predicted dust lifting. Finally in Section 6 we provide a summary.

2. Model description

The MarsWRF GCM is the Mars-specific, global implementation of the planetWRF model (Richardson et al., 2007), based on the National Center for Atmospheric Research (NCAR) terrestrial Weather Research and Forecasting (WRF) model (Skamarock and Klemp, 2008), which was created as a replacement for the now-obsolete NCAR MM5 mesoscale model. WRF was designed to be cross-platform compatible and to operate on modern massively parallel (shared and non-shared memory) supercomputers. Richardson et al. (2007) described modifications to WRF to enable global and planetary usage, and presented initial simulations. The globalization of WRF undertaken in the development of planetWRF has now been adopted and improved by NCAR and is now available as a part of the public WRF release (www.wrf-model.org). The planetary modifications, with full physical parameterizations included for the specific example case of Mars, are available at www.planetwrf.com.

For this study, the MarsWRF GCM has been set up largely as described by Richardson et al. (2007). Radiative heating rates are provided by wide band representations of CO_2 gas and dust in the visible and infrared (IR) as described in Richardson et al. (2007), and referred to as the WBM (“wide band model”) radiative transfer option in MarsWRF. Within this radiative scheme, thermal IR heating and cooling associated with CO_2 is treated following Hourdin (1992) and with dust following Haberle et al. (1982). Overlap of absorption and emission within the 15 μm band between dust and CO_2 is ignored. In the solar band, the scheme considers heating due to CO_2 (following Forget et al., 1999) and dust (following Briegleb, 1992). Dust opacity in the atmosphere for both the thermal infrared and solar bands is prescribed following an updated version of the Mars Climate Database spatial and temporal distribution (Lewis et al., 1999; Montmessin et al., 2004). Simulations in this work use the ‘MGS’ dust scenario from the Mars Climate Database (Montmessin et al., 2004). Spatially variable surface properties (topographic height, surface roughness, albedo, thermal inertia, and emissivity) come from Mars Orbiter Laser Altimeter and Thermal Emission Spectrometer observations (Smith and Zuber, 1996; Garvin et al., 1999; Christensen et al., 2001; Putzig and Mellon, 2007). Surface maps of topography, roughness length, albedo, and thermal inertia sampled at three different model resolutions used in this paper are shown in Fig. 1. A CO_2 cycle is implemented using a simplified scheme in which atmospheric CO_2 condensation is always deposited directly on the surface (i.e., no CO_2 ice clouds are allowed to form). The temperature of the surface is calculated using a multi-level implicit heat conduction model that captures both the diurnal and seasonal waves. Energy balance at the surface considers heating from the radiative transfer model described above, subsurface heat conduction, latent heat associated with CO_2 phase change, and sensible heat exchange with the atmosphere. The sensible heat exchange occurs in the surface layer that is part of the model’s planetary boundary layer (PBL) parameterization scheme, and the simulations presented here use the “YSU” PBL model option (Troen and Mahrt, 1986; Hong and Pan, 1996; Noh et al., 2004; Hong et al., 2006).

The MarsWRF GCM has already been validated against atmospheric temperature data and compared against other global models (Richardson et al., 2007; Mischna and Wilson, 2008). On the basis of these comparisons, the MarsWRF GCM performs similarly to other current Mars models. Guo et al. (2009) undertook a detailed study of the MarsWRF GCM CO_2 cycle and lander surface pressure records and showed that with an appropriate choice of the polar ice properties, the Viking Lander annual pressure cycles could be fit to within instrument error. Lee et al. (2009) used the MarsWRF GCM to simulate tidal signatures in the zonal mean day-side and night-side temperature retrievals from the Mars Climate Sounder (MCS), extending the validation of the model with data to roughly 80 km. Most recently, the MarsWRF GCM has been used within and to provide a demonstration of a data assimilation system (Lee et al., 2011) based on the NCAR Data Assimilation Research Testbed (DART) (Anderson et al., 2009). The data assimilation results also suggest that the MarsWRF GCM can adequately simulate the martian climate, though with errors mostly associated with the evolution of the seasonal ice caps and the distribution of atmospheric aerosols.

At mid- and high-latitudes, like most grid-point GCMs, the MarsWRF GCM attempts to maintain a timestep based on the equatorial grid spacing by including a zonal filter (of Fourier transform wavenumber modes) that aims to compensate for the decreasing zonal grid spacing with latitude. Equatorward of 45° latitude there is no filtering. Between 45° and 60° the filter preferentially damps zonal modes whose wavelength is shorter than twice the equivalent zonal grid spacing at the equator (Takacs and Balgovind, 1983). This filter damps these shorter wavelength modes but does not eliminate them. Poleward of 85°, if the given model resolution includes any points at these latitudes, a hard

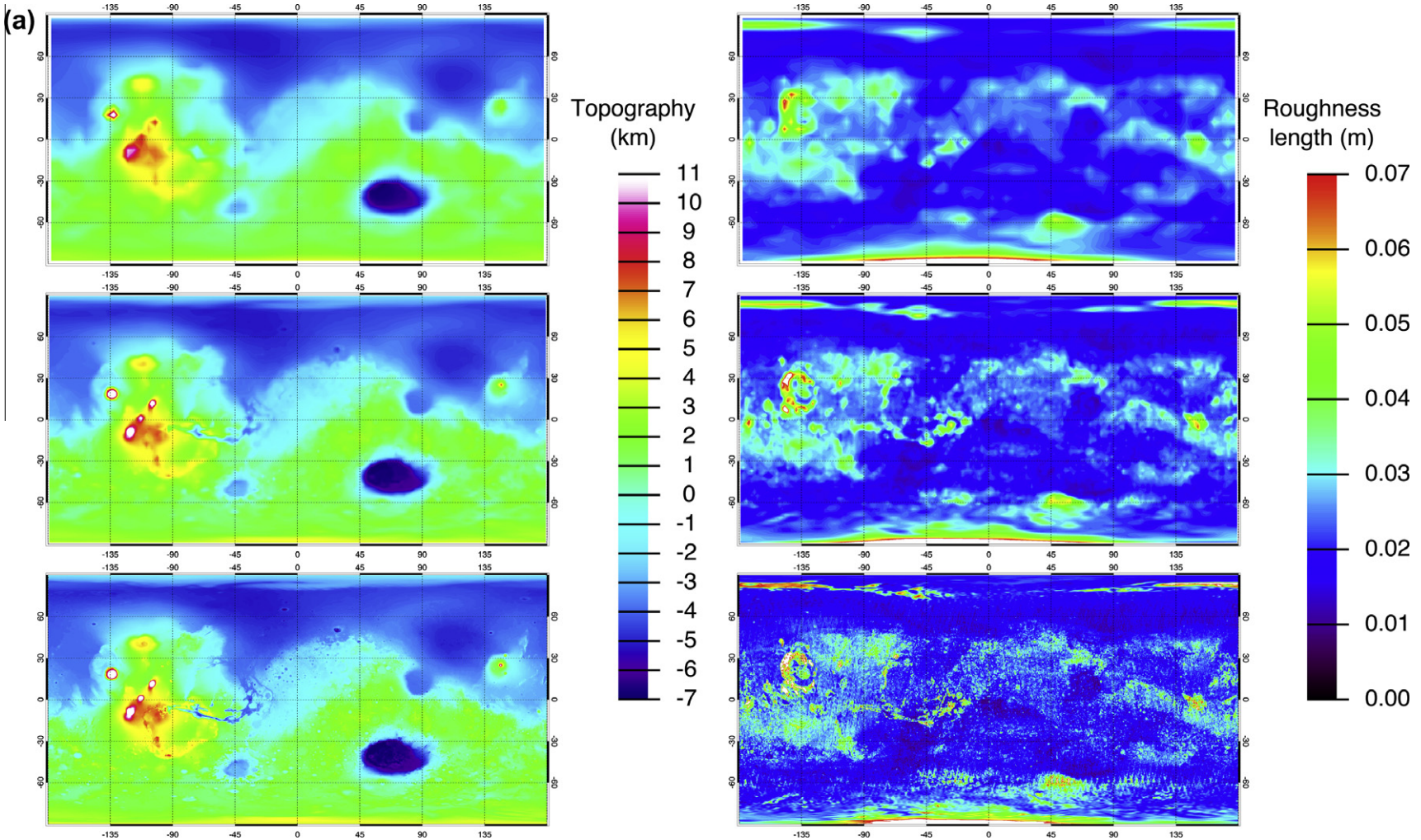

Fig. 1. Surface fields used as lower boundary conditions for the MarsWRF simulations in this study showing the effect of resolution. From left to right, the columns show: (a) surface topography and roughness length; (b) albedo and thermal inertia. The colorbar references for each field are to the right of each column. Rows in every column represent three different resolutions discussed in this paper: from top to bottom, standard resolution (SR, 5° × 5°), high resolution (HR, 2° × 2°), and global mesoscale (GM, ½° × ½°). These cases are listed in Table 2 and further described and defined in Section 3 of the text. (For interpretation of the references to color in this figure legend, the reader is referred to the web version of this article.)

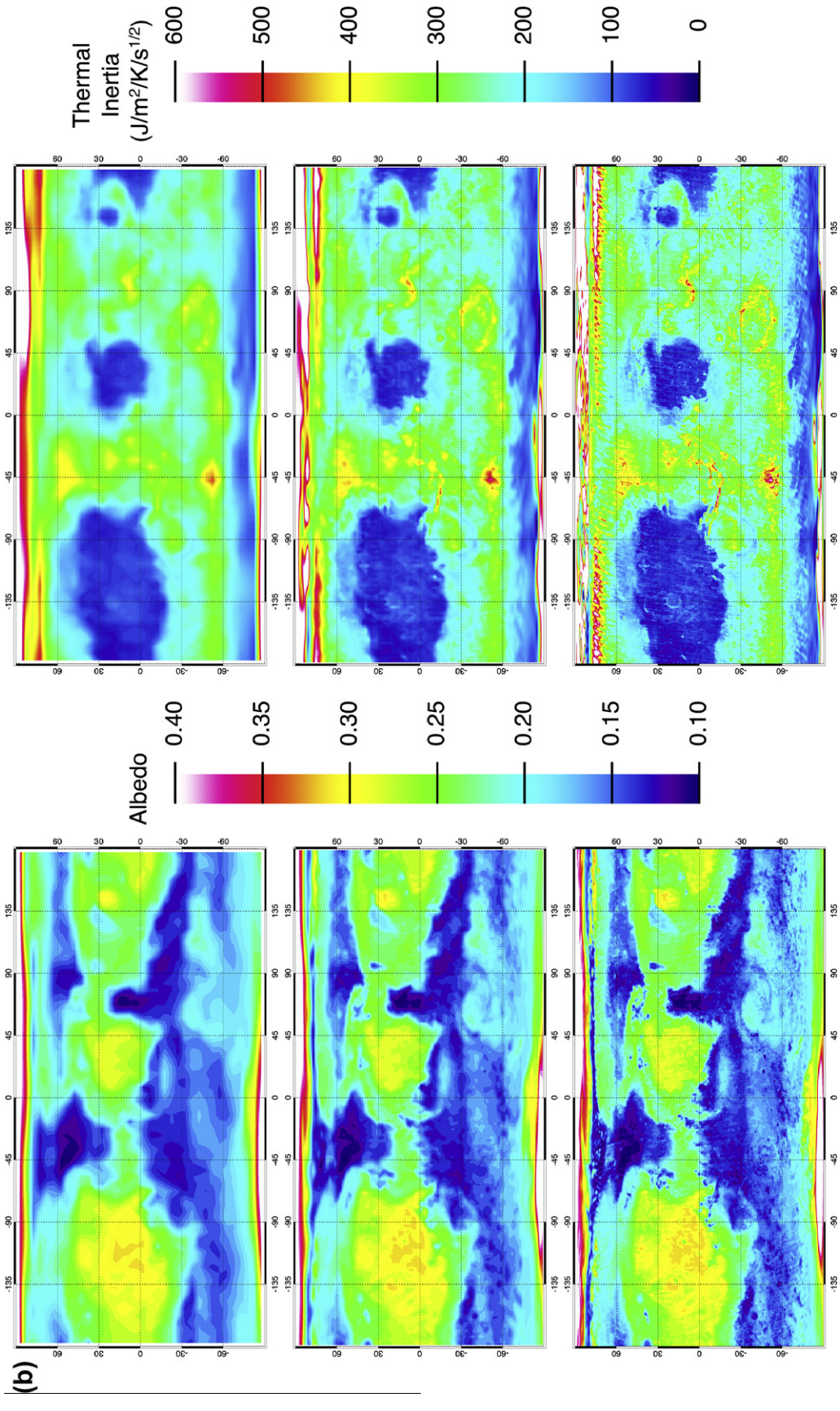

Fig. 1. (*continued*)

Table 1
Eta values for the MarsWRF GCM vertical layer centers used in this study. Here, Eta = $(P - P_{top})/(P_{surf} - P_{top})$, where P is the layer center (hydrostatic equilibrium) pressure, P_{surf} is the local surface pressure, and P_{top} is a fixed model top pressure (Laprise, 1992). In these simulations $P_{top} \approx 5$ mPa. The layer locations are based on the 40-layer model of Wilson and Hamilton (1996).

Layer number	Eta value	Layer number	Eta value
1	0.9906	21	0.02791
2	0.9604	22	0.02125
3	0.9106	23	0.01613
4	0.8463	24	0.01220
5	0.7721	25	0.009194
6	0.6926	26	0.006899
7	0.6113	27	0.005152
8	0.5312	28	0.003827
9	0.4546	29	0.002824
10	0.3832	30	0.002070
11	0.3181	31	0.001504
12	0.2599	32	0.001081
13	0.2092	33	7.646×10^{-4}
14	0.1664	34	5.280×10^{-4}
15	0.1314	35	3.526×10^{-4}
16	0.1031	36	2.251×10^{-4}
17	0.08025	37	1.348×10^{-4}
18	0.06207	38	7.303×10^{-4}
19	0.04772	39	3.377×10^{-4}
20	0.03655	40	9.557×10^{-4}

cutoff that completely eliminates these short wavelength modes is applied. Between 60° and 85°, the two filter modes are blended with a weighting that is linear in latitude. In both cases, the filter reference wavenumber scales as resolution is changed (i.e., so as to admit higher wavenumber waves as the resolution is increased).

The simulations described in the remainder of this paper were all performed using a 40-level vertical grid based on that used in the GFDL Mars GCM (Wilson and Hamilton, 1996). The vertical eta levels are equivalent to the more common sigma levels under the hydrostatic equilibrium assumption, as is typical for GCMs (Laprise, 1992). The eta levels used in these simulations are shown in Table 1.

3. Effects of resolution on the simulation of the global atmosphere

In order to assess the effect of resolution on the global circulation, we have undertaken four identical simulations with MarsWRF where only the horizontal grid spacing is changed (see also Table 2): (a) 7.5° × 9° latitude by longitude (low resolution case, "LR"), (b) 5° × 5° (standard resolution case, "SR"), (c) 2° × 2° (high resolution case, "HR") and finally (d) 0.5° × 0.5° (global mesoscale resolution case, "GM"). The first three simulations (LR, SR, HR) were carried out for three years, with the last year being included in this study. The final simulation (GM) was too large to productively run for an entire year, and so was only integrated for 100 martian days, starting just before southern summer solstice (at a solar longitude, L_s, of roughly 260°) from an initial condition that was interpolated from the steady state HR case at that season. This season was chosen as it exhibited the greatest variation in behavior as resolution was increased in the lower resolution cases. The surface forcing fields were also adjusted for the resolution in each of these cases, and maps of the topography, surface roughness length, albedo, and thermal inertia are shown for the SR, HR, and GM cases in Fig. 1. Throughout this paper, we have used the standard terrestrial definitions of season and the standard martian definition of solar longitude. Thus, northern spring is assumed to begin at northern spring equinox ($L_s = 0°$) and proceed to the northern summer solstice ($L_s = 90°$). Consequently, seasonal phrases like "early northern spring" should be taken to mean $L_s \approx 0$–30°, and "late northern spring" to mean $L_s \approx 60$–90°.

3.1. Zonal mean cross sections

The zonal mean temperatures and zonal winds for northern autumnal equinox and both solstices are shown in Fig. 2. Overall, each case displays the same large-scale features. For southern summer solstice ($L_s = 270°$), the simulations all show a strong polar front in the northern mid-and-high latitudes that tilts poleward with altitude, a temperature maximum that is near the surface in the southern mid-to-high latitudes, and a tropical temperature minimum at the top of the model. This is as we would expect given that the lower resolution models are able to capture the broad features seen in zonal temperature cross sections from Mariner 9 Infrared Interferometer Spectrometer (IRIS), Mars Global Surveyor (MGS) Thermal Emission Spectrometer (TES), and Mars Reconnaissance Orbiter (MRO) Mars Climate Sounder (MCS).

In detail, however, Fig. 2 shows significant trends in structure from lowest to highest resolution cases. The impact of resolution changes is different for the three seasons shown.

3.1.1. Northern winter solstice ($L_s = 270$–300°)

From the surface to about 150 Pa (roughly 15 km) the circulation appears similar across all resolution cases. However, above this level to the top of the model there is a distinct change in the structure that is amplified as horizontal resolution is increased. In the LR case, the northward meridional flow increases nearly uniformly with height above about 50 Pa (about 25 km). The edge of the polar front and equivalently the polar vortex tilts poleward smoothly with height.

As the resolution is increased to the SR case, the meridional circulation above 50 Pa splits into two distinct poleward flows, one peaking around 5–10 Pa and the other above 0.1 Pa. These mean meridional flows are coincident with a tightening of the polar front/vortex at these levels, producing a distinct poleward "pinch" of the polar vortex at about 20 Pa and an equatorward expansion at about 0.2 Pa. In general, the temperature maximum, representing the adiabatic heating in the downwelling within the polar vortex wall has become even better defined in the SR versus the LR run.

In the HR case, the twin meridional jets above 50 Pa become better defined even than in the SR case, with the upper troposphere meridional jet concentrated near 10 Pa. The poleward tightening of the vortex at this level also becomes slightly more apparent. Above this, the equatorward expansion of the westerlies between the

Table 2
List of MarsWRF GCM simulations used in this study, along with the model grid spacing, the simulation name and "nickname," and comments.

Simulation name (and "nickname")	Meridional spacing (°)	Zonal spacing (°)	Comment
Low Resolution (LR)	7.5	9	Leovy and Mintz (1969), Pollack et al. (1990) and Haberle et al. (1993)
Standard Resolution (SR)	5	5	Roughly typical for most current GCMs
High Resolution (HR)	2	2	
Global Mesoscale (GM)	0.5	0.5	Maximum of 30 km grid spacing
High Meridional Resolution Test (HRM)	2	5	High meridional and standard zonal resolution
High Zonal Resolution Test (HRZ)	5	2	High zonal and standard meridional resolution

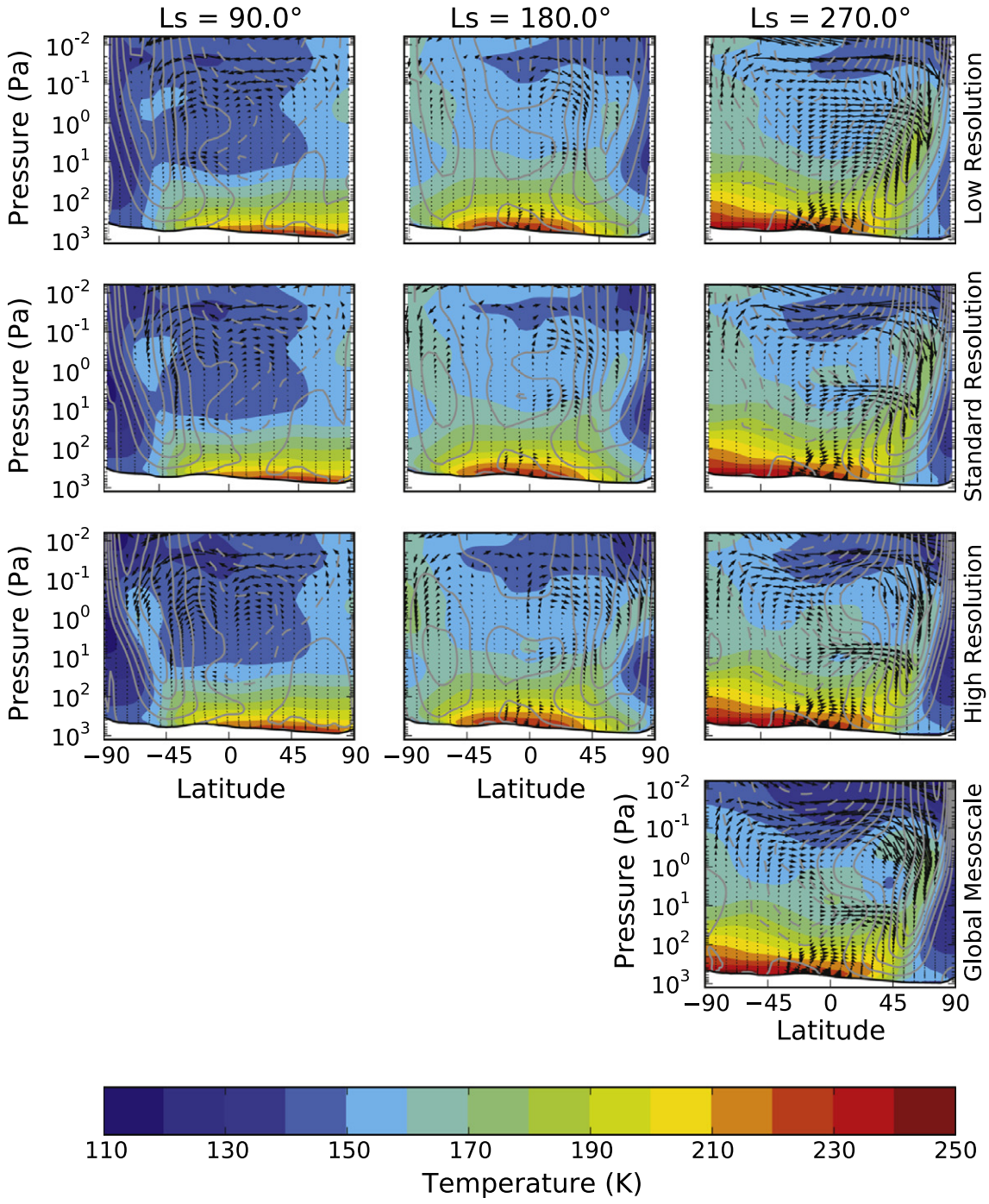

Fig. 2. Time average zonal mean temperatures (color), zonal winds (contours) and meridional circulation (arrows) for northern summer solstice, northern autumnal equinox, and northern winter solstice (columns, left to right) and for the low resolution (LR), standard resolution (SR), high resolution (HR), and global mesoscale (GM) simulations (rows, top to bottom). The time averaging is over 30° of L_s centered on L_s = 90°, 180°, and 270°, respectively from left to right. Note that the GM case is only shown for northern winter. Case resolutions are as defined in the text and in Table 2. (For interpretation of the references to color in this figure legend, the reader is referred to the web version of this article.)

meridional jets becomes much more dramatic. The tongue of warm temperatures that forms the polar front/vortex wall is also further concentrated in latitude. These changes between the HR and SR cases all represent further developments of the same changes that were seen between the SR and LR case. Another feature that could arguably be noticed in the comparison of SR and LR runs, but becomes very apparent in the HR run, is the development of an equatorial temperature maximum at roughly 1 Pa. This appears to be associated with zonal mean descent over the southern tropics between about 0.5 and 5 Pa. This feature is consistent with MCS temperature retrievals for southern summer (shown in McCleese et al. (2010) and especially Fig. 8 of Heavens et al. (2011)), and appears to be a dayside feature with no nightside equivalent, strongly suggesting a thermotidal origin.

For the northern winter solstice period, the GM simulation is also available for comparison. This simulation shows the same features as the HR case, except that the poleward side of the polar front is even further sharpened, and the presumably tidally moderated mean flow descent at 1–10 Pa in the tropics and above 1 Pa in the mid and high northern latitudes is intensified leading to

stronger local temperature maxima at about 8 Pa and 0°N, and about 0.3 Pa and 60°N, respectively. Both the vortex wall and the polar front now exhibit a distinct lower and middle atmosphere behavior, potentially more consistent with the MCS observations (Heavens et al., 2011), with a primary westerly jet core maximum at about 10 Pa, local westerly jet core minima at about 1 Pa, and an increasing westerly jet again above this level. Local vortex wall temperature maxima and minima correspond to the jet speed minima and maxima, respectively.

3.1.2. Southern winter solstice (L_s = 90–120°)

The northern summer atmosphere displays less resolution dependence than that of southern summer. The major features of the circulation, including the vertical splitting of the winter jet and the meridional poleward flow in the winter hemisphere (the

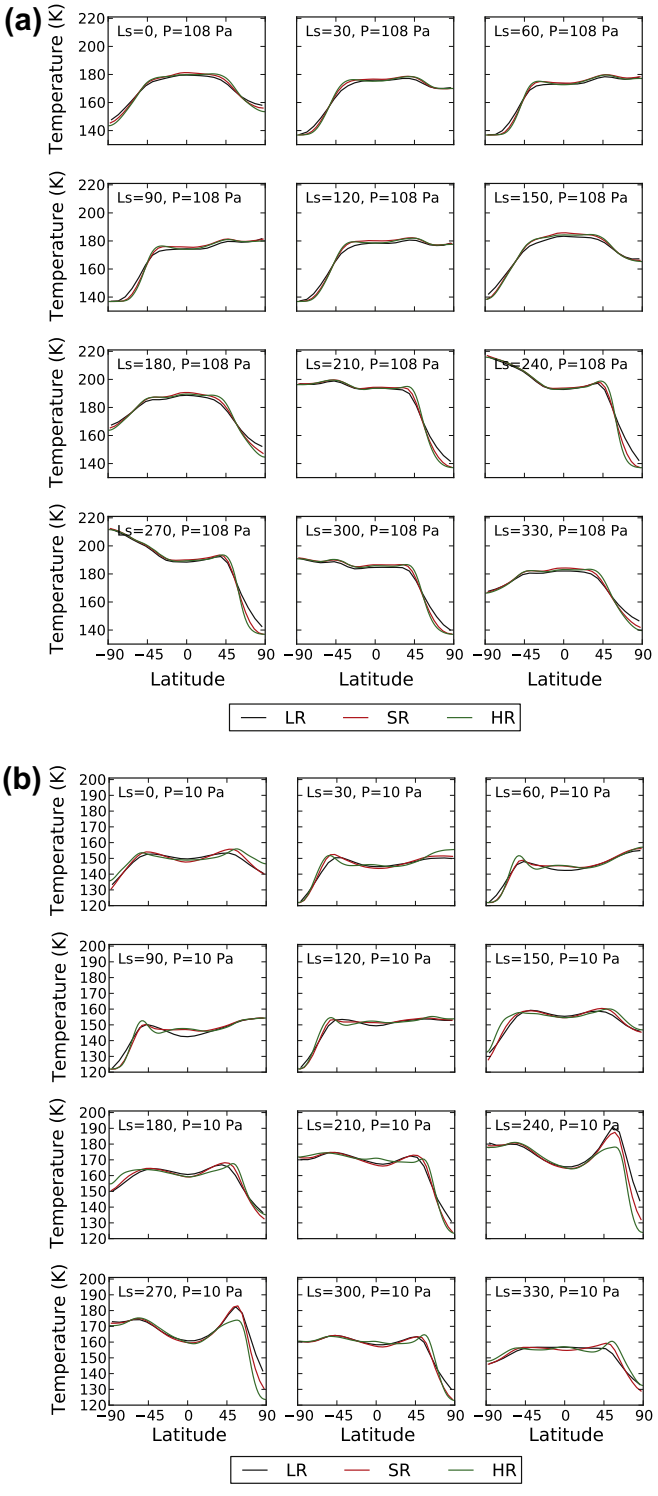

Fig. 3. Zonal mean atmospheric temperatures for the low resolution (LR), standard resolution (SR) and high resolution (HR) cases averaged over 30° of L_s centered on the L_s indicated on each panel. Panel (a) shows output from 108 Pa (roughly 17 km altitude). Panel (b) shows output from 10 Pa (roughly 40 km altitude).

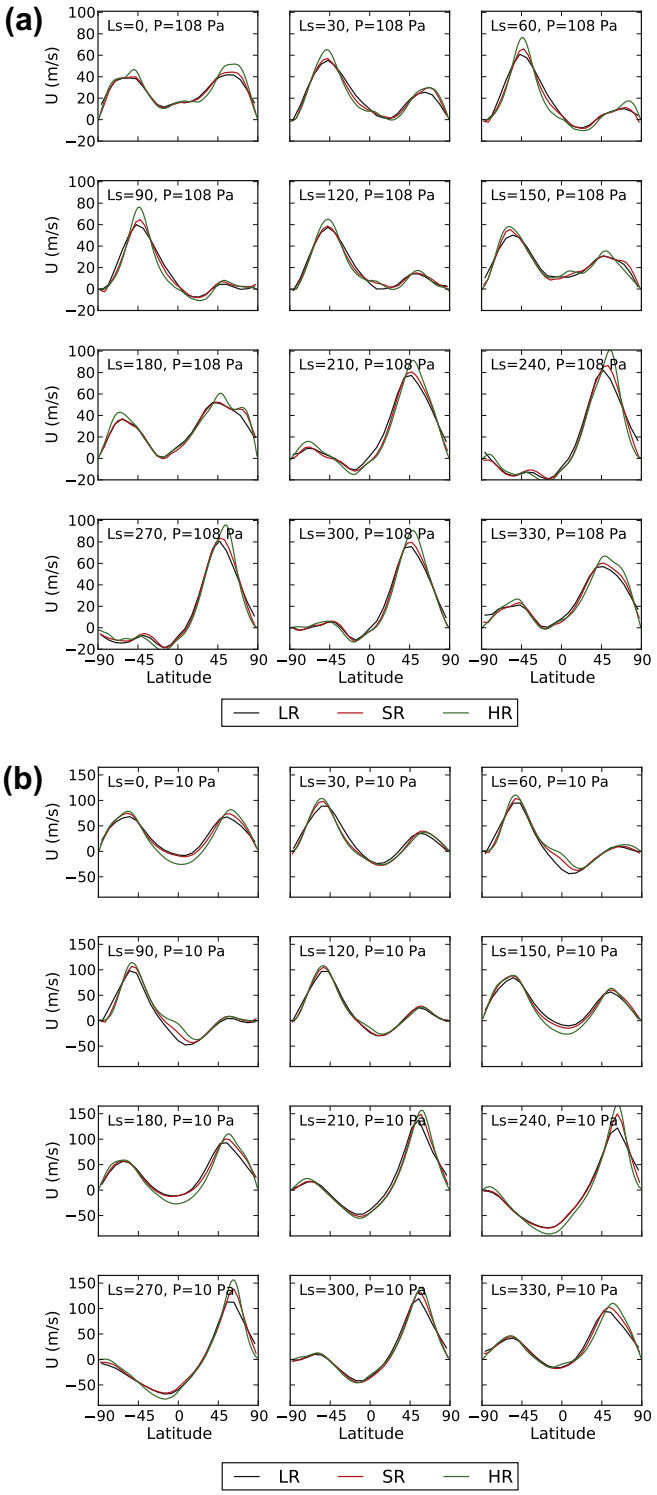

Fig. 4. Same as Fig. 3 but for the zonally averaged zonal wind.

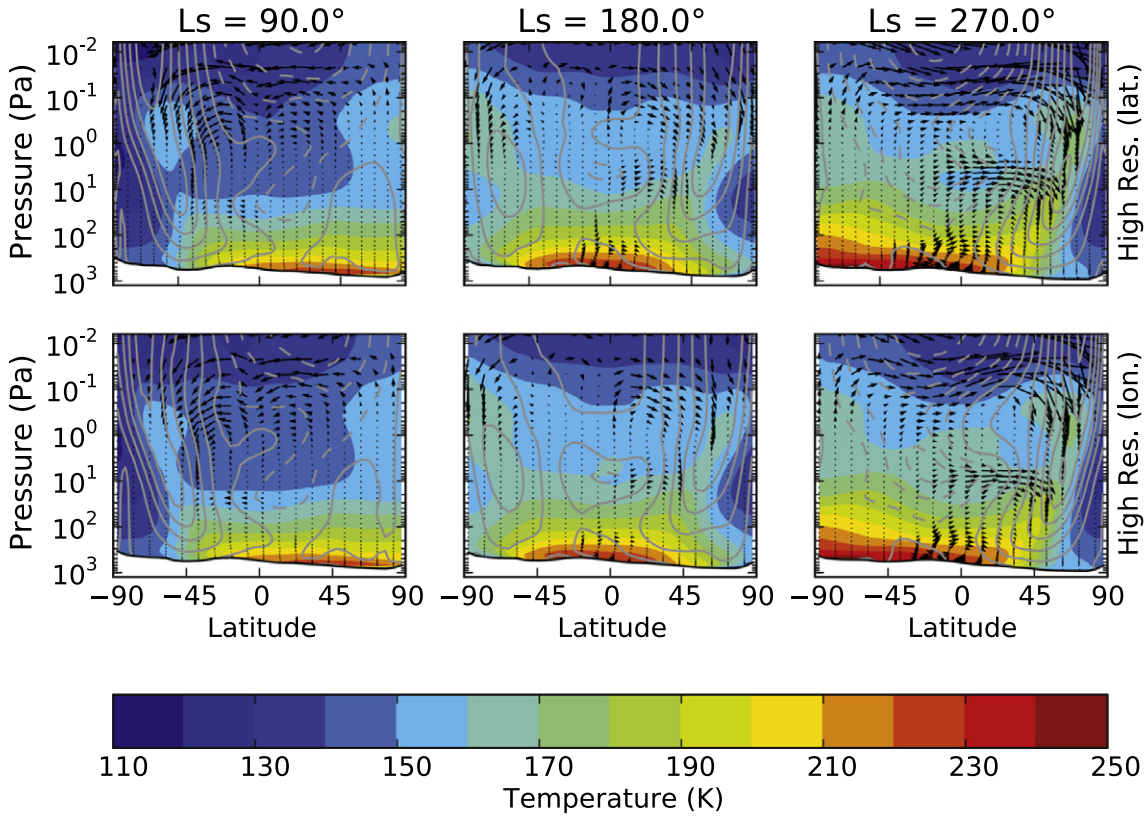

Fig. 5. Same as Fig. 2 except that the rows correspond to the High Resolution Meridional (HRM or High Res. (lat)) and the High Resolution Zonal (HRZ or High Res. (lon)) cases. See text and Table 2 for details.

seasonal "mirrors" of features that appear in the SR and higher resolution cases for southern summer) are already present in the LR case for northern summer solstice. The major change with resolution (LR to HR) is focused on the strength and sharpness of the winter polar front and polar vortex wall. As the resolution is increased, the vortex wall decreases in latitudinal extent (sharpens) and the temperature maximum at altitudes above about 1 Pa is intensified and also more latitudinally confined. The maximum above 1 Pa is rather detached in the LR case, but forms a near continuous thermal "wall" by the HR case. This corresponds to an increase in the polar front temperature maximum and results from an increase in downward vertical motion along the vortex wall. As with the southern summer case, there is good argument for at least partial separation of the circulation at altitudes above about 5 Pa from that below (as argued from MCS data by Heavens et al. (2011)). It should be noted that none of the simulations are able to reproduce the magnitude of the upper level temperature maximum over the winter pole (MarsWRF is cooler than observed by about 10 K) or the full penetration of the maximum directly over the geographical pole. These problems are apparently common to all current grid-point models (McCleese et al., 2008), though it should be noted that the HR is substantially closer to observations than the LR case.

3.1.3. Northern autumnal equinox (L_s = 180–210°)

The northern autumnal equinox shows little resolution sensitivity at altitudes below about 1 Pa. Above this level, the circulation involves mean upwelling over the equator and mean descent over the poles. As the resolution is increased, the location of the downwelling shifts poleward and intensifies. Over the southern pole, this corresponds to higher temperatures in a relatively broad depth range centered at about 1 Pa (and directly over the geographic pole). Over the northern pole, the polar temperature maximum is not only increased with increasing resolution, but the maximum is pushed significantly poleward, bringing peak temperatures from about 60°N for the LR case to directly over the pole for the HR case. The temperature pattern derived from the HR simulation is in much better agreement with MCS observations than the LR case, although peak temperatures at these levels remain over 10 K cooler than observed (McCleese et al., 2010).

3.2. Changes in the polar front and polar vortex

The changes in the polar front and vortex with resolution can be better quantified by examining the full seasonal evolution of the zonal mean temperatures and zonal mean winds on selected isobaric levels. Figs. 2 and 3 show these values as a function of latitude for 12 seasonal windows, for all the model resolution cases examined, and at 10 Pa and 108 Pa.

Considering the lower atmosphere first (108 Pa, roughly 17 km), the temperature structure in the tropics and summer hemispheres (Fig. 3a) varies little with resolution (as was also apparent in the zonal mean sections, Fig. 2). In the winter hemisphere, only the LR case performs consistently differently from the other cases, showing a weaker extra-tropical temperature gradient. While this is obvious in the southern winter, it is a much larger effect in northern winter. At equinox, both poles show a weaker temperature gradient in the LR case.

Via the thermal wind relationship, the weaker winter polar temperature gradients in the LR case manifest as weaker and slightly equatorward-displaced westerly jet peaks (Fig. 4a). In northern winter, the jet speed at 108 Pa can differ by up to 20 m/s between the LR and HR cases in the seasonal mean. Interestingly, while the subtle differences in the temperature structure in the

winter poles was harder to discern between the SR and HR case, the jet structure shows a more continuous progression from weaker and more equatorward to stronger and more poleward jet peaks as the resolution increases from LR to SR to HR cases.

In the middle atmosphere (10 Pa, roughly 42 km), there is somewhat more variation in temperatures between resolution cases as compared to the lower atmosphere (Fig. 3b), in all cases with a monotonic trend (e.g., if a temperature is lower at a point in the SR case compared to the LR case, it will be even lower in the HR case). At equinox, the temperature maximum moves to higher latitudes as the resolution increases, while the temperatures right at the pole tend to be similar or decrease, thus the HR case shows a stronger gradient right at the pole. Again, this is reflected in the winds via the thermal wind relation, with stronger polar jets with increasing resolution (Fig. 4b).

From mid northern spring to mid northern summer (L_s = 30–120°), early southern spring (L_s = 210°), and mid southern summer (L_s = 300–330°), but not southern summer solstice (L_s = 270°), the HR case shows a temperature maximum at the equator at the 10 Pa level. The other cases show a minimum at this level. This maximum appears to be associated with daytime adiabatic heating of air descending into the concentrated poleward meridional jet (discussed in Section 3.1). The maximum does not appear at southern solstice because at this season the descent into this poleward jet occurs at levels above 10 Pa.

At winter mid latitudes and high latitudes at southern summer solstice at upper levels, high temperatures are pressed further inwards towards the pole but with lower peak temperatures. For L_s = 240°, the peak temperatures are about 190 K for the LR case, but roughly 175 K for the HR case, displaced poleward by about 10° of latitude in the HR case. The temperature trend is opposite that seen at the winter pole at northern summer solstice, where peak temperatures both increase and move poleward. A possibility for the difference in behavior with resolution increase is that while in the northern summer, the winter circulation simply seems to intensify, in southern summer the winter hemisphere circulation undergoes the transition from 'single' to 'double' poleward jets as the resolution is increased (Section 3.1). An increasing fraction of the poleward and descending motion occurs below 10 Pa and consequently results in a temperature decrease with increased spatial resolution. Despite the decreasing trend of peak temperatures at 10 Pa, the winter jet strength is seen to increase with resolution at both solstices, with an almost 40 m/s difference between the LR and HR cases at L_s = 240°. This is likely the effect of integrating stronger temperature gradients at lower levels in the HR case.

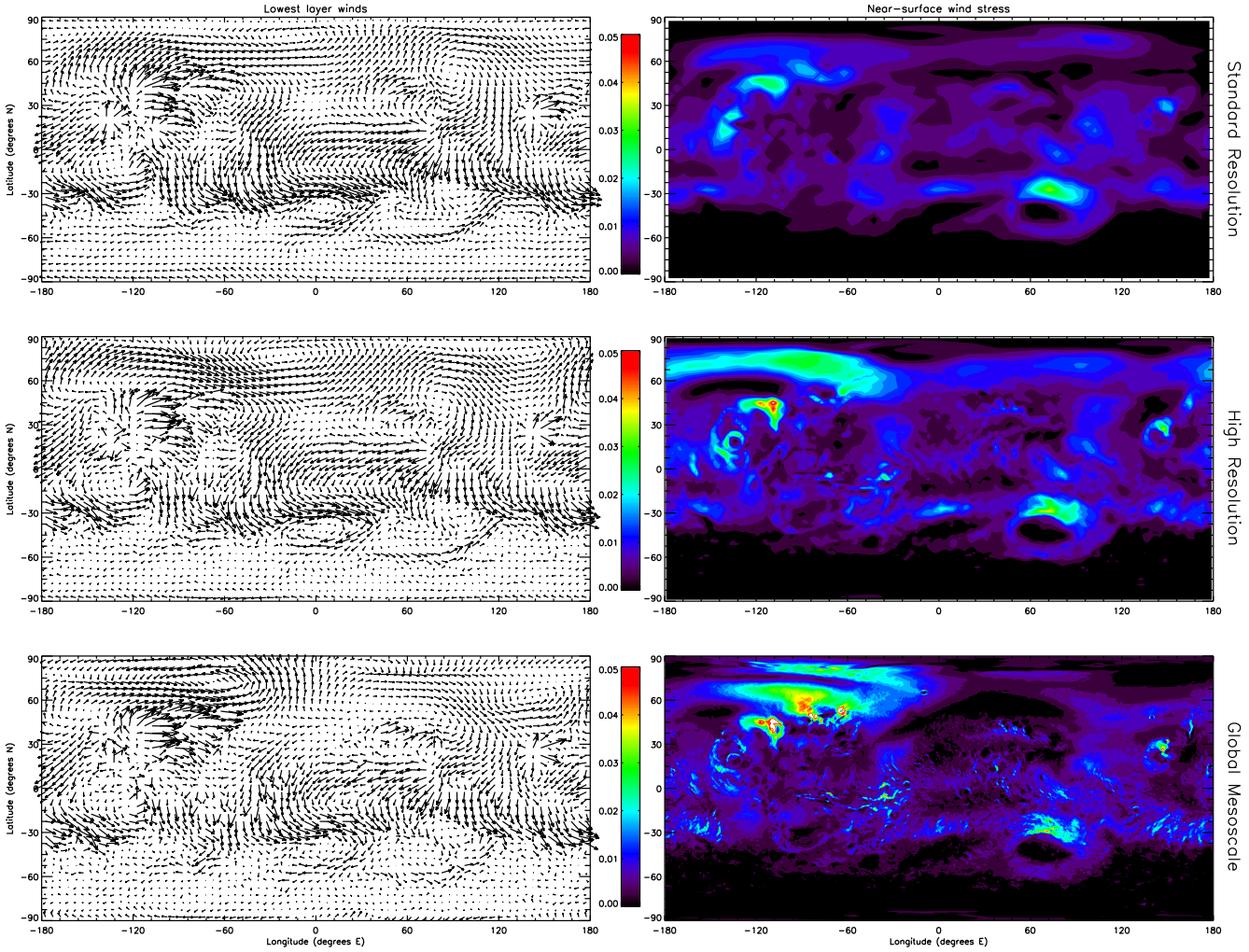

Fig. 6. Surface winds and surface wind stresses for northern winter solstice. Surface winds are indicated by arrows where the direction and magnitude represent the modeled horizontal wind vector (left panels). The surface winds for the higher resolution cases are only shown at the LR case grid point spacing for purposes of figure readability, and their values have been interpolated to the LR grid point locations. The total wind stress in Pa is indicated in the right hand panels. The standard resolution (SR – top row), high resolution (HR – middle row), and global mesoscale (GM – bottom row) cases are shown. The output have been averaged over one martian day.

4. Frontal versus wave resolution study

The changes in the strength and location of the polar front and corresponding polar jet with resolution could plausibly be related to either model resolution of the polar front or the model resolution of waves (or both). The former is plausible because the thermal gradient at the polar front is sufficiently sharp that the lower model resolutions may simply not resolve it. The latter is plausible as higher frequency waves and/or instabilities that are unresolved in the lower resolution cases may have a significant impact on the zonal mean circulation at higher resolutions (and hence possibly in the real atmosphere). A simple test to elucidate the qualitative relative importance of these distinct (and potentially interconnected) aspects of resolution can be performed by constructing hybrid standard/high resolution cases in which either the meridional resolution or the zonal resolution has been doubled from the SR case (the HRM and HRZ cases, respectively). With the High Resolution Meridional (HRM) case, we enable better resolution of the polar jet and thermal gradient while retaining the SR case zonal resolution of eddies. With the High Resolution Zonal (HRZ) case, we enable better zonal resolution of eddies while retaining the SR case resolution of meridional gradients. Zonal mean results from these cases are shown in Fig. 5.

Comparing the zonal wind structure at $L_s = 270°$ from the SR and HR cases (Fig. 2) with the HRM and HRZ case (Fig. 5), we note that the majority of the large-scale changes between the SR and HR cases can be explained by changing the zonal resolution alone. The HRZ case looks very similar to the HR case, suggesting that the zonal resolution of eddies is crucial to the generation of the increased "pinching" of the polar jet and the corresponding increased vertical confinement of mid-latitude meridional jets at 10 Pa and above 0.1 Pa (as produced between the SR and HR cases, see Section 3.1.1). By contrast, the HRM case looks very similar to the SR case, which suggests that the increased meridional resolution of this case does not significantly change the simulated circulation at this season. In fact, the only noticeable change from SR to HRM is a very mild increase in the polar jet core temperature maximum near 1 Pa that seems to result from slightly stronger downwelling with better meridional resolution.

In southern winter, the SR and HR cases were only marginally different, and this lack of significant change with resolution is also attested in the HRM and HRZ cases. There is arguably a slight meridional tightening of the polar vortex wall expressed in the HRZ case and not in the HRM case, suggesting a very marginal role of higher frequency eddies. Otherwise the southern winter is rather insensitive to resolution.

At northern autumnal equinox, the SR to HR transition was primarily marked by the extension of the northern polar temperature maximum to directly over the pole just above 1 Pa (Section 3.1.3). Fig. 5 hints that this transition may primarily be associated with higher meridional resolution (HRM displaying more of the polar connection of the temperature maximum than HRZ). This may suggest the importance of an extra poleward grid point in the HRM and HR cases versus the SR and HRZ cases.

5. The impact of resolution on surface winds, surface wind stresses, and dust lifting

Much of the motivation for higher resolution simulations of the martian atmosphere is provided by the desire to better capture topographic forcing. The relatively thin atmosphere and large topographic range yield a greater influence of local up-slope/down-slope, sea breeze, and topographic deflection on near-surface winds for Mars than for Earth (e.g. Burk, 1976; Siili et al., 1999; Rafkin et al., 2001; Toigo and Richardson, 2002; Tyler et al., 2002). While the large-scale surface wind structure is broadly defined by the propagation of global thermal tides and the separation between trade/monsoonal winds (i.e., the surface manifestation of the "Hadley" or tropical mean overturning circulation) at low latitudes and winter westerlies at high latitudes (e.g., Greeley et al., 1993), large scale topography imposes steady zonal structure through the generation of "gyres" with strong boundary currents (Joshi et al., 1995), with higher resolution yielding additional and substantial deviations from the mean (e.g., see Fig. 6).

For simulation of local-scale phenomena, such as dune-forming winds and dust devils, and lander wind measurements, it has long been recognized that higher resolution, in the form of mesoscale simulations, is desirable (e.g. Rafkin et al., 2001; Toigo and Richardson, 2002; Toigo et al., 2003; Fenton et al., 2005). What has been less clear is whether resolution of smaller-scale aspects of the circulation is of consequence for the large-scale circulation. In the prior sections we examined this question from the perspective of the zonal mean thermal and wind structure. Here, we focus on the impact of model resolution on surface winds and dust lifting. For example, do lower-resolution models provide a statistically useful representation of the dust lifting predicted in higher resolution models, or indeed that occurs on Mars itself?

5.1. Surface winds and stresses at southern summer solstice

As a first examination of surface wind stresses and dust lifting variations with model resolution, we show diurnally averaged surface winds and stresses at southern summer solstice for the SR, HR, and GM cases in Fig. 6. For clarity, we have not included the LR case, as it is very similar to the SR case in most respects. This day is typical of surrounding days, and although the pattern of dust lifting varies with season, the basic results are representative of other times of year. Overall there are strong similarities in the spatial distribution of high wind stress between the three cases. The SR case is very similar to a spatial average of either the HR or GM cases, the only significant differences being in the high northern (winter) latitudes where the timing of the passage of low-pressure storm systems causes case-to-case differences (this is purely

Table 3
Variation of global dust lifting quantities for two model resolutions, eight dust lifting stress thresholds, and for both the Fryberger (1979) and White (1979) method of dust flux estimation (see text). Units of lifting are arbitrary, but identical for the two runs and eight thresholds. Note that in the first row, corresponding to zero threshold, the lifting flux reduces to a cubic dependence on the drag velocity and is hence identical regardless of which method is used.

Threshold stress ($N\ m^{-2}$)	SR case; Fryberger method	HR case; Fryberger method	Ratio of HR to SR (Fryberger)	SR case; White method	HR case; White method	Ratio of HR to SR (White)
0	5450	5330	0.98	5450	5330	0.98
0.007	1250	1240	0.99	3340	3280	0.98
0.014	389	396	1.02	1190	1200	1.01
0.021	120	131	1.09	392	423	1.08
0.028	37.1	45.7	1.23	126	153	1.21
0.035	11.4	16.5	1.45	40.2	56.7	1.41
0.042	3.43	6.09	1.78	12.3	21.3	1.73
0.049	1.02	2.35	2.30	3.72	8.36	2.25

an artifact of our using a single daily average from each case). The location and magnitude of peak stresses north of Hellas (20–30°S, 50–100°E), in the southern summer ITCZ (the intertropical convergence zone, i.e., the surface-level location of convergence and upwelling in the tropical mean overturning circulation) (15°S–5°N, 60–30°W), near the Tharsis and Elysium volcanoes (0–50°N, 150–110°W; 20–35°N, 140–160°E), and at locations along the dichotomy boundary are very similar in all three simulations. In general, the low-resolution pattern of stress is similar whether we average the high-resolution wind stresses or whether we simulate the stresses resulting from low-resolution topography.

The detail that emerges in the transition from the SR to GM cases is correlated with topography (cf. Figs. 1 and 6). Although this may seem obvious, terrestrial experience has shown that variations in wind stresses can be associated with small-scale effects such as thermal and albedo contrasts, or the random distribution of storms and convective systems (seen to some extent here at high northern latitudes). However, as suggested by prior mesoscale simulations of Mars, the effect of topography is dominant. Emerging clearly in the surface wind stress patterns in the GM case are resolution-limited topographic features (cf. Figs. 1 and 6) such as: the walls of Valles Marineris (0–20°S, 100–30°W), the Thaumasia Highlands (the extended ridge south of Solis Planum, 30–45°S, 110–60°W), the Argyre basin (45–60°S, 60–30°W), numerous individual craters (Lomonosov, 65°N, 9°W, and Mie, 48°N, 140°E, craters are easily identified in the northern plains), and the detailed lower reaches of Elysium Mons.

5.2. Dust lifting

GCMs parameterize many atmospheric processes happening at scales less than the grid point resolution. But certain processes are more sensitive to the resolution chosen, in particular those that are non-linear and those that involve threshold effects, as both of these are more sensitive to the atmospheric state predicted at a given point. Dust lifting is a process that exhibits both traits. Estimates of the dust flux injected via saltation of sand particles typically depend non-linearly on the near-surface wind, with a roughly cubic dependence on the drag velocity (a function of the surface wind stress) at the surface. In addition, injection only occurs when the surface wind stress exceeds a threshold value to initially mobilize the sand particles.

While it is known that GCM dust lifting schemes need to be "retuned" as resolution is increased, the effects of model resolution on dust lifting have not been explicitly examined. Hence in this study, we present the first quantitative look at how simulations of dust lifting would vary with resolution and the threshold value for saltation.

Table 3 shows the global dust lifting quantity for a martian year for the SR and HR cases, for eight different values of the saltation threshold, and as calculated with the Fryberger (1979) and White (1979) formulations. The Fryberger (1979) formulation can be written as:

$$Dust\ lifted \propto \rho(u^*)^3\left(1-\frac{u^*_{thresh}}{u^*}\right)\Delta t$$

while the White (1979) formulation can be written as:

$$Dust\ lifted \propto \rho(u^*)^3\left(1-\frac{u^*_{thresh}}{u^*}\right)\left(1+\frac{u^*_{thresh}}{u^*}\right)^2\Delta t$$

where ρ is near-surface air density, Δt is timestep, u^* is drag velocity, and u^*_{thresh} is the threshold drag velocity, which in these experiments is calculated for a series of constant threshold wind stresses, τ_{thresh}, via the relationship $u^*_{thresh} = \sqrt{(\tau_{thresh}/\rho)}$. For all values in Table 3, the total amount lifted was summed for an entire Mars year (following a year of model spin-up) with the instantaneous drag velocity and density values at each timestep and the above formulations for eight different threshold stress values. Dust accumulations were recorded with sufficient numerical precision to avoid the round-off errors that could result from adding tiny increments to a large running total.

The results tabulated in Table 3 show one main effect. For a given method of lifting calculation and for low wind stress thresholds, the lower resolution (SR) and higher resolution (HR) cases show nearly identical total annual global dust lifting amounts. However, as the stress threshold is increased, the HR case yields higher total dust lifting quantities, reaching about 125% more annual lifted dust than in the SR case (i.e., 2.25 times that of the SR case). Increasing the dust lifting threshold effectively removes the lower drag velocity contributions to the dust lifting function, thus increasing the weighting on the higher values. The HR case better captures the high wind stress tail of the power spectrum by representing locations of high wind stress due to the resolution of sharper topographic gradients.

A footnote to this discussion is the minor point that at zero threshold (as well as the next lowest threshold), the total amount of dust lifted is actually lower in the HR than the SR case (albeit only by less than 3%). This very modest excess of dust amount lifted in the SR case cannot be due to differing resolution of the same atmospheric state since higher resolution will always yield identical or higher lofted amounts. In other words, if the SR and HR cases were merely different discrete samplings of the *same* continuous atmospheric state, then the HR sampling would be mathematically constrained to always produce equal or greater dust lifting. For completeness, we include a brief and idealized example of this in Appendix A. Note that the amount of dust lifted would be identical only in the unlikely case of there being no wind variance at scales smaller than the resolution of the SR case (equivalent to $\Delta = 0$ in Appendix A). The result for the lowest thresholds in Table 3 therefore tells us that the SR case must generate very slightly higher overall drag velocity magnitudes than the HR case. The small reduction in total amount of dust lifted with resolution was found to be repeatable over several simulations. It is not immediately obvious why the total amount of dust lifted is reduced with increased resolution, and this suggests a topic to be examined in more detail in future work.

6. Summary and conclusions

The purpose of this study was to provide an initial survey of the impact of horizontal resolution on the simulation of the martian global atmosphere and climate. Typically, global models have tended to use 5–10° meridional resolution, and while limited area models (e.g., mesoscale or large eddy simulations) have been used on scales all the way down to meters, the effects of resolution on the global circulation and large-scale dust lifting have not been summarized.

The primary findings are:

1. The general circulation, as defined by the gross-scale representation of jets and the mean overturning circulation, are qualitatively well simulated at lower resolution. In most aspects, the structure of the general circulation does not change significantly with the factor of 15 (linear) increase in resolution examined here, with the exception of the details discussed below.
2. The structure and magnitude of the northern polar winter jet changes significantly between our LR and HR cases (and consistently with increased resolution). While represented as a single, reasonably smooth jet present throughout most of

the atmosphere at low tesolution, the jet is seen to "split" vertically as resolution is increased. Specifically, the jet shows greater latitudinal extent and weakening of peak speeds in the lower atmosphere (between the surface and roughly 10 Pa) and in the middle atmosphere (between 10 and 0.1 Pa), with a distinct narrowing of the jet at 10 Pa and above 0.1 Pa.

3. The splitting of the northern polar winter jet is coincident with the development of two distinct meridional jets between the equator and roughly 45° (at 10 Pa) and from roughly pole-to-pole at upper levels. These jets can be visualized as the upper level branches of lower atmosphere ("Hadley") and middle atmosphere mean overturning circulations.
4. There is a hemispheric asymmetry in the sensitivity of the winter polar circulation to resolution, with the southern polar winter atmosphere exhibiting the split structure at all resolutions considered.
5. The hemispheric asymmetry of resolution sensitivity is also present in the equinoctial atmosphere, where the thermal maximum defining the northern polar front extends much more completely to the pole as the resolution is increased.
6. Increasing model resolution improves the simulation of the northern polar atmosphere, as revealed by Mars Climate Sounder retrievals, at both northern winter solstice and at equinox.
7. The relative insensitivity of the southern winter polar jets to resolution suggests that model resolution may not be a key factor for improving model simulations of argon confinement (Sprague et al., 2004; Lian et al., 2012), at least from the perspective of simulation of the atmospheric dynamics (as opposed to tracer transport, which is not considered here).
8. The variation of the northern polar vortex structure with resolution appears to be primarily sensitive to zonal resolution and thus to the representation of waves (and hence wave-mean flow interactions) rather than the resolution of the polar front (meridional) gradient.
9. Our results suggest that modeling studies of northern autumn and winter eddies (waves and storms) should take into account the resolution sensitivity of the background wind and thermal structure. For example, mesoscale models of cyclogenesis embedded in low resolution GCM simulations will not be exposed to the same mean background structure as a global mesoscale model. On the other hand, this is not significantly the case in the south.
10. The time-average near-surface wind patterns on a large scale are not particularly sensitive to resolution (i.e., no major reconfiguration of the surface wind field occurs as a result of increasing resolution).
11. The vast majority of changes in surface wind stress patterns with increased resolution can be considered as the linear superposition of large-scale wind patterns and local scale circulations due to topography (e.g., craters, volcanoes, canyons, etc.).
12. Predictions of dust emission as a function of resolution show insensitivity to resolution in the absence of a stress threshold for lifting, but show a significant increase with increased resolution as the threshold is increased. At higher resolution, the model captures and simulates more topography-driven small-scale circulations with an associated increase of upper range of wind speeds and peak wind stresses. Thus as the threshold increases toward the tail of the spectrum, only the higher resolution simulations contain wind stresses sufficiently high to produce lifting. Combined with the roughly cubic dependence on drag velocity, this produces far more dust lifting in the higher resolution simulations as the threshold is increased.
13. If these simulations were repeated including the radiative effects of suspended dust, the predominantly positive feedbacks on further lifting seen in those types of experiments (e.g., Newman et al. (2002)) leads us to believe that an even greater bias toward increased lifting at increased resolution for high threshold stresses would be seen.

Acknowledgments

A.D.T. was supported by Planetary Atmospheres grant NNG06GH27 and by the Johns Hopkins University Applied Physics Laboratory Stuart S. Janney Publication Fellowship Program. C.E.N., C.L. and M.I.R. were supported by Planetary Atmospheres grant NNX10AB42G. Model simulations were undertaken on the NASA High End Computing Pleiades system. We wish to thank NCAR for their ongoing support of the terrestrial Weather and Research Forecasting (WRF) model.

Appendix A

In the limiting case of no lifting threshold, both lifted dust flux formulations (Fryberger, 1979; White, 1979) reduce to a linear dependence on density and time interval and a cubic dependence on the drag velocity, and consequently the first row of results in Table 3 are identical for the two methods. The tendency for the lower resolution model to predict more dust lifting than the higher resolution case is the opposite of what one would expect purely due to resolution of an otherwise identical atmospheric state. It is easy to show that the higher resolution case ought to predict more lifting, as follows. Consider two different representations of the same total area (A): one represents the area with a single grid box (and hence a single representative drag velocity for the whole area) while the other resolves the area with two equally sized boxes (and hence two drag velocity values contributing with equal weighting to the lifting). We assume the air density and the time increment considered in both cases are equal. If we also assume that the two grids are representing the same true system state, merely sampling it at different levels of resolution, then the lifting quantity in the lower resolution domain, L_{low}, is effectively that resulting from the average of the drag velocities in the higher resolution domain:

$$L_{low} \propto A\rho(u^*_{avg})^3\Delta t = A\rho\left(\frac{u^*_1+u^*_2}{2}\right)^3\Delta t$$

The lifting quantity summed over the higher resolution domain, L_{high}, is the sum of the lifting over the two higher resolution boxes:

$$L_{high} \propto \frac{A\rho}{2}(u^{*3}_1+u^{*3}_2)\Delta t$$

If the drag velocity is uniform across the area (A) considered in both cases, then $L_{low} = L_{high}$. If instead there is a variation in drag velocity across the domain, then this will not be the case. The simplest example is one where:

$$u^*_1 = u^* + \delta u^* \quad \text{and} \quad u^*_2 = u^* - \delta u^*,$$

which ensures that the domain mean remains the same as the prior example. Then we find that:

$$L_{low} \propto A\rho u^{*3}\Delta t \quad \text{and} \quad L_{high} \propto A\rho u^{*3}\Delta t + 3A\rho u^*\delta u^2\Delta t$$
$$= L_{low} + 3A\rho u^*\delta u^2\Delta t$$

This merely illustrates the fact that since the lifting rate function is cubic in drag velocity, the function tends to put greater weight on being able to resolve higher peak drag velocities within the domain. It should be noted that while we have shown a highly simplified example for clarity, the result is completely general.

References

Anderson, J. et al., 2009. The Data Assimilation Research Testbed a community facility. Bull. Am. Meteorol. Soc. 90, 1283–1296.

Briegleb, B.P., 1992. Delta-Eddington approximation for solar radiation in the NCAR community climate model. J. Geophys. Res. 97, 7603–7612.

Burk, S.D., 1976. Diurnal winds near the Martian polar caps. J. Atmos. Sci. 33, 923–939.

Christensen, P.R. et al., 2001. Mars Global Surveyor Thermal Emission Spectrometer experiment: Investigation description and surface science results. J. Geophys. Res. 106, 23823–23871.

Fenton, L.K., Toigo, A.D., Richardson, M.I., 2005. Aeolian processes in Proctor Crater on Mars: Mesoscale modeling of dune-forming winds. J. Geophys. Res. 110, 2004JE002309.

Forget, F. et al., 1999. Improved general circulation models of the martian atmosphere from the surface to above 80 km. J. Geophys. Res. 104 (E10), 24155–24175.

Fryberger, S.G., 1979. Dune forms and wind regime. In: McKee, E.D. (Ed.), A Study of Global Sand Seas, USGS Professional Paper, vol. 1052. US Geological Survey and United States National Aeronautics and Space Administration, Washington, DC, pp. 137–169.

Garvin, J.B., Frawley, J.J., Abshire, J.B., 1999. Vertical roughness of Mars from the Mars Orbiter Laser Altimeter. Geophys. Res. Lett. 26, 381–384.

Greeley, R., Skypeck, A., Pollack, J.B., 1993. Martian aeolian features and deposits: Comparison with general circulation model results. J. Geophys. Res. 98, 3183–3196.

Guo, X., Lawson, W.G., Richardson, M.I., Toigo, A., 2009. Fitting the Viking lander surface pressure cycle with a Mars general circulation model. J. Geophys. Res. 114, 2008JE003302.

Haberle, R.M., Leovy, C.B., Pollack, J.B., 1982. Some effects of global dust storms on the atmospheric circulation of Mars. Icarus 50, 322–367.

Haberle, R.M. et al., 1993. Mars atmospheric dynamics as simulated by the NASA/Ames general circulation model I. The zonal mean circulation. J. Geophys. Res. 98, 3093–3124.

Heavens, N.G., McCleese, D.J., Richardson, M.I., Kass, D.M., Kleinböhl, A., Schofield, J.T., 2011. Structure and dynamics of the martian lower and middle atmosphere as observed by the Mars Climate Sounder: 2. Implications of the thermal structure and aerosol distributions for the mean meridional circulation. J. Geophys. Res. 116, 2010JE003713.

Hong, S.-Y., Pan, H.L., 1996. Nonlocal boundary layer vertical diffusion in a medium-range forecast model. Mon. Wea. Rev. 124, 2322–2339.

Hong, S.-Y., Noh, Y., Dudhia, J., 2006. A new vertical diffusion package with an explicit treatment of entrainment processes. Mon. Wea. Rev. 134, 2318–2341.

Hourdin, F., 1992. A new representation of the absorption by the CO_2 15-μm band for a martian general circulation model. J. Geophys. Res. 97, 18,319–18,335.

Joshi, M.M., Lewis, S.R., Read, P.L., Catling, D.C., 1995. Western boundary currents in the martian atmosphere: Numerical simulations and observational evidence. J. Geophys. Res. 100, 5485–5500.

Laprise, R., 1992. The Euler equations of motion with hydrostatic-pressure as an independent variable. Mon. Wea. Rev. 120, 197–208.

Lee, C. et al., 2009. Thermal tides in the martian middle atmosphere as seen by the Mars Climate Sounder. J. Geophys. Res. 114, 2008JE003285.

Lee, C. et al., 2011. Demonstration of ensemble data assimilation for Mars using DART, MarsWRF, and radiance observations from MGS TES. J. Geophys. Res. 116, 2011JE003815.

Leovy, C.B., Mintz, Y., 1969. Numerical simulation of the atmospheric circulation and climate on Mars. J. Atmos. Sci. 26, 1167–1190.

Lewis, S.R. et al., 1999. A climate database for Mars. J. Geophys. Res. 104, 24177–24194.

Lian, Y., Richardson, M.I., Newman, C.E., Lee, C., Toigo, A.D., Mischna, M.A., Campin, J.-M., 2012. The Ashima/MIT Mars GCM and argon in the martian atmosphere. Icarus 218, 1043–1070.

McCleese, D.J. et al., 2008. Intense polar temperature inversion in the middle atmosphere on Mars. Nat. Geosci. 1, 745–749.

McCleese, D.J. et al., 2010. Structure and dynamics of the martian lower and middle atmosphere as observed by the Mars Climate Sounder: Seasonal variations in zonal mean temperature, dust, and water ice aerosols. J. Geophys. Res. 115, 2010JE003677.

Michaels, T.I., Colaprete, A., Rafkin, S.C.R., 2006. Significant vertical water transport by mountain-induced circulations on Mars. Geophys. Res. Lett. 33. http://dx.doi.org/10.1029/2006GL026562.

Mischna, M.A., Wilson, R.J., 2008. The Mars General Circulation Model Intercomparison Study, Third International Workshop on the Mars Atmosphere: Modeling and Observations, held November 10–13, 2008 in Williamsburg, Virginia. LPI Contribution No. 1447, 9088.

Montmessin, F., Forget, F., Rannou, P., Cabane, M., Haberle, R.M., 2004. Origin and role of water ice clouds in the martian water cycle as inferred from a general circulation model. J. Geophys. Res, 109, 2003JE002284.

Newman, C.E., Lewis, S.R., Read, P.L., Forget, F., 2002. Modeling the martian dust cycle 2. Multiannual radiatively active dust transport simulations. J. Geophys. Res. 107, 2002JE001920.

Noh, Y., Chun, W.G., Hong, S.Y., Raasch, S., 2004. Improvement of the k-profile model for the planetary boundary layer based on large eddy simulation data. Bound. Layer Meteorol. 107, 401–427.

Pollack, J.B., Haberle, R.M., Schaeffer, J., Lee, H., 1990. Simulations of the general circulation of the martian atmosphere: 1. Polar processes. J. Geophys. Res. 95, 1447–1473.

Putzig, N.E., Mellon, M.T., 2007. Apparent thermal inertia and the surface heterogeneity of Mars. Icarus 191, 68–94.

Rafkin, S., Haberle, R., Michaels, T., 2001. The Mars regional atmospheric modeling system: Model description and selected simulations. Icarus 151, 228–256.

Rafkin, S.C.R., Sta Maria, M.R.V., Michaels, T.I., 2002. Simulation of the atmospheric thermal circulation of a martian volcano using a mesoscale numerical model. Nature 419, 697–699.

Richardson, M.I., Toigo, A.D., Newman, C.E., 2007. PlanetWRF: A general purpose, local to global numerical model for planetary atmospheric and climate dynamics. J. Geophys. Res. 112, 2006JE002825.

Siili, T., Haberle, R.M., Murphy, J.R., Savijärvi, H., 1999. Modeling of the combined late-winter ice cap edge and slope winds in Mars' Hellas and Argyre regions. Planet. Space Sci. 47, 951–970.

Skamarock, W.C., Klemp, J.B., 2008. A time-split non-hydrostatic atmospheric model for Weather Research and Forecasting applications. J. Comput. Phys. 227 (7), 3465–3485.

Smith, D.E., Zuber, M.T., 1996. The shape of Mars and the topographic signature of the hemispheric dichotomy. Science 271, 184–188.

Sprague, A.L. et al., 2004. Mars' south polar Ar enhancement: A tracer for south polar seasonal meridional mixing. Science 306, 1364–1367.

Takacs, L.L., Balgovind, R.C., 1983. High-latitude filtering in global grid-point models. Mon. Wea. Rev. 111, 2005–2015.

Toigo, A.D., Richardson, M.I., 2002. A mesoscale model for the martian atmosphere. J. Geophys. Res. 107, 2000JE001489.

Toigo, A.D., Richardson, M.I., Ewald, S.P., Gierasch, P.J., 2003. Numerical simulation of martian dust devils. J. Geophys. Res. 108, 2002JE002002.

Troen, I., Mahrt, L.A., 1986. A simple-model of the atmospheric boundary-layer-sensitivity to surface evaporation. Bound. Layer Meteorol. 37 (1–2), 129–148.

Tyler Jr., D., Barnes, J.R., Haberle, R.M., 2002. Simulation of surface meteorology at the Pathfinder and VL1 sites using a Mars mesoscale model. J. Geophys. Res. 107, 2001JE001618.

White, B.R., 1979. Soil transport by winds on Mars. J. Geophys. Res. 84, 4643–4651.

Wilson, R.J., Hamilton, K., 1996. Comprehensive model simulation of thermal tides in the martian atmosphere. J. Atmos. Sci. 54, 1290–1326.